ELSEVIER

Contents lists available at ScienceDirect

### Computers in Biology and Medicine

journal homepage: www.elsevier.com/locate/compbiomed





# A computational model of tsDCS effects in SOD1 mice: from MRI-based design to validation

L. de Oliveira Pires <sup>a,\*,1</sup>, B. Wasicki <sup>b,1</sup>, A. Abaei <sup>c</sup>, J. Scekic-Zahirovic <sup>d</sup>, F. Roselli <sup>d,e,2</sup>, S. Fernandes <sup>a,2</sup>, M. Baczyk <sup>b,2</sup>

- a Instituto de Biofísica e Engenharia Biomédica, Faculdade de Ciências da Universidade de Lisboa, Campo Grande, Lisbon, 1749-016, Portugal
- <sup>b</sup> Poznań University of Physical Education, Department of Neurobiology, Poland
- <sup>c</sup> Core Facility Small Animal Imaging, Ulm University, Ulm, 89081, Germany
- <sup>d</sup> German Center for Neurodegenerative Diseases (DZNE)-Ulm, Ulm, 89081, Germany
- e Dept. of Neurology, Ulm University, Ulm, 89081, Germany

### ARTICLE INFO

Keywords:
Spinal computational model
MRI
In vivo electrophysiology
Neuromodulation
Amyotrophic lateral sclerosis

### ABSTRACT

During trans-spinal direct current stimulation (tsDCS) the transmembrane potential of neurons is modified by an electric field (EF) induced due to externally applied direct current (DC). The resultant functional effects are being harnessed in the treatment of various neurological conditions; however, the fundamental mechanisms of action underlying tsDCS remain unclear. This ambiguity is largely attributed to the limited knowledge of the geometrical constraints of the EF in the polarized spinal regions. It is, then, essential to develop tools that enable researchers to plan tsDCS approaches in a controlled and systematic manner, ensuring the reproducibility of stimulation effects at spinal targets.

With this paper, we aim to provide a comprehensive computational model of tsDCS intervention in mice to support further fundamental research in this area. Our model was constructed using high-resolution MRI scans of C57/B6 mice, which were segmented and reconstructed into a realistic mouse computational model. *In vivo* electrophysiological measurements of voltage gradients in SOD1 G93A mice were used to validate our model predictions in real-life scenarios. In both the modeling and *in vivo* studies, we employed a rostrocaudal arrangement of DC electrodes to replicate stimulation parameters that have proven effective for modulating murine spinal circuits.

Both the computational and  $in\ vivo$  approaches yielded highly consistent results, with EF parameters primarily influenced by the distance between the target site and the tsDCS electrodes. We conclude that this developed model offers high accuracy in EF distribution and can significantly substantiate basic research in tsDCS.

### 1. Introduction

Trans-spinal direct current stimulation (tsDCS) is a non-invasive neuromodulatory technique that involves applying low-intensity direct currents (DC) to the spinal cord through electrodes placed in the skin [1–3]. This stimulation method induces electric fields in the spinal cord that can transiently change the transmembrane potential of spinal neurons and synaptic communication [4]. Despite a growing number of evidence on the therapeutic potential of tsDCS to modulate motor function [5,6], pain-related responses [7,8] and neurological functions

in individuals with spinal cord injury or other spinal disorders [9,10], the physiological and mechanistic explanation of tsDCS action remains elusive.

TsDCS effects are known to be polarity-dependent, i.e. these depend on the position of the anode and cathode relative to the neural target of interest. For instance, tsDCS can evoke a differential impact on spinal responses, such as the H-reflex, according to the orientation of the induced current density, as observed in previous studies [11–13]. However, current polarity cannot explain all tsDCS effects, as discrepancies exist in the direction of the effects (facilitation vs. inhibition)

E-mail address: ldpires@ciencias.ulisboa.pt (L. de Oliveira Pires).

<sup>\*</sup> Corresponding author.

 $<sup>^{1}</sup>$  Co-first Author.

 $<sup>^{2}</sup>$  Co-senior Author.

depending on the applied research model. For example, animal studies showed that in wild-type (WT) mice, anodal (depolarizing) tsDCS increases the excitability of Ia afferents providing excitatory input to spinal motor neurons (MNs), while cathodal (hyperpolarizing) tsDCS does not produce a significant effect [14]. In contrast, in WT cats, it is cathodal polarization that increases the afferent activity, while anodal polarization produces an inhibitory effect [15]. In human applications, anodal tsDCS increases the vertical jump performance in healthy individuals [16], while at the same time decreasing the nociceptive flexion reflex response [17]. These discrepancies can arise from several factors, affecting the current spread within the spinal cord, which result in different spatial distributions of the electric field at the target site. Cellular responses due to direct current stimulation were demonstrated to vary with electric field orientation [18], therefore is critically important to establish the geometrical constraints of tsDCS-evoked current spread to fully account for its variability in the upcoming mechanistic investigations of tsDCS actions. This is an essential approach for designing tsDCS interventions in neurological conditions in which directional changes in neuronal activity can have beneficial or detrimental effects on cell survival, such as Amyotrophic Lateral Scle-

Computational models based on finite element (FE) approaches provide critical insights into the geometric constraints of multiple biological therapeutic scenarios [21–24], including DC stimulation [25–27]. These are essential tools to understand the biophysics of non-invasive DC in electrically excitable tissues using a virtual environment. In the context of tsDCS, these models allow detailed investigations on the electric field induced by tsDCS in the spinal cord, additionally contributing to optimize current delivery at target. Model-guided approaches thus provide a solid background to guide the design of clinical tsDCS protocols towards specific clinical purposes [28, 29].

In this paper, we aim to provide a detailed computational model to predict the electric fields (EF) induced by tsDCS in the SOD1 G93A (henceforth SOD1 mice) mouse model of ALS which replicates the human ALS phenotype [30]. In SOD1 mice, alterations in spinal MN synaptic excitation/inhibition balance, coupled with abnormal cells' intrinsic properties form the hallmark of disease pathophysiology [31–34] and tsDCS has already been shown to affect both the spinal MN intrinsic excitability [35,36] and synaptic actions converging on these cells [14].

Considering this and the usefulness of FE-based computer models, the proposed *in silico* model will be based on super-resolution MRI scans of C57/B6 mice, anatomically similar to SOD1 G93A mice, to provide highly precise predictions of DC electric field induced at the spinal cord. This will be verified through direct intraspinal recordings obtained *in vivo*. The methodology presented here provides a solid framework that can be utilized for optimizing tsDCS protocols, while additionally aiding in the investigation of the mechanistic effects of tsDCS in ALS, combined with robust *in vivo* studies in SOD1 mice.

### 2. Methods

### 2.1. Mice MRI acquisition

All MRI imaging was performed ex vivo under the animal experimentation license no. 1522 issued by the Regierungspraesidium Tübingen. Three C57/B6 mice at postnatal day 30 (PND 30) were transcardially perfused with phosphate-buffered saline (PBS, 1.5 mL/g body weight) followed by fixation with 4 % paraformaldehyde (PFA) in PBS (1.5 mL/g body weight). After fixation, each mouse was immersed in inert, fluorocarbon-based Fluorinert (FC-43, IoLiTec GmbH) and positioned carefully within a custom-designed polycarbonate tube, specifically engineered for precise alignment within the cryogenically-cooled MRI coil. The tube was completely filled with pre-cooled Fluorinert (4 °C) while ensuring no air bubbles remained.

MRI scans were performed using an ultra-high-field 11.7 T small animal MRI system (BioSpec 117/16, Bruker BioSpin, Ettlingen, Germany) equipped with a 9 cm gradient insert (BGA-S9) and operated with ParaVision 7.0.0 (Fig. 1). For whole-body imaging, a 60 mm birdcage quadrature volume resonator was utilized for both excitation and signal reception. To optimize image clarity, motion averaging and fat suppression modules were applied, and field-of-view (FOV) saturation and flip-back modules were activated for the T<sub>2</sub>-RARE sequences.

Two different MRI sequences were selected for their complementary imaging properties. The Fast Low Angle Shot (FLASH) sequence was chosen for its excellent  $T_2^*$ -weighted imaging capabilities, ideal for visualizing tissue interfaces and structures with susceptibility contrast. The FLASH sequence parameters were: TR/TE = 1800/4.25 ms, flip angle =  $25.0^\circ$ , matrix size =  $250\times230$ , spatial resolution =  $100\times100\times350~\mu\text{m}^3$ , bandwidth = 65.8~kHz, and 150~signal averages, resulting in a total imaging duration of approximately 17 h and 15 min. This sequence acquired 165 axial slices.

In contrast, the Rapid Acquisition with Relaxation Enhancement (RARE) sequence was selected for clear  $T_2$ -weighted anatomical detail, providing improved contrast between fluids and surrounding soft tissues. Two  $T_2$ -RARE sequences were conducted, sharing common parameters: TR/TE =18000/32 ms, echo spacing =10.667 ms, RARE factor =8, in-plane spatial resolution  $=100\times100~\mu\text{m}^2$ , slice thickness  $=350~\mu\text{m}$ , and bandwidth =98.7~kHz. Each sequence had an acquisition time of approximately 17 h and 55 min. These sequences differed only in orientation and FOV:

- 1. Axial imaging:  $FOV = 25 \times 23 \text{ mm}^2$ , 165 slices acquired.
- 2. Coronal imaging:  $FOV = 59 \times 23 \text{ mm}^2$ , 50 slices acquired.

### 2.2. Computational realistic modeling of tsDCS effects in mice

### 2.2.1. MRI segmentation and 3D modeling

The open-source software tool ITK-SNAP (www.itksnap.org) was used to segment the MRI scans of one male mouse selected from the datasets obtained in 2.1 [37]. The segmentation process involved semi-automatic techniques, specifically active contour methods and a threshold-based approach to isolate multiple anatomical regions. The segmented regions included skin, vertebrae, sacrum, ilium, intervertebral discs, white matter (WM) and gray matter (GM) of the spinal cord (SC), and several visceral organs (brain, heart, lungs, stomach, liver, spleen, pancreas, and intestines). The segmentation of the thoracic vertebrae included a residual representation of the ribs.

The obtained tissue masks were converted into 3D surface meshes and exported as.stl files to Blender 4.0, an open-source 3D creation suite (www.blender.org/), for further 3D modeling. In Blender, we performed manual corrections and used tools such as smoothing, remeshing and boolean operations, to ensure that the surfaces were refined and that the modeled regions did not intersect. Additional anatomical structures were created based on the initial segmentations. Specifically, the cerebrospinal fluid (CSF) was modeled with a 0.04 mm offset from the WM, and the dura mater with a 0.03 mm offset from the CSF. These thickness values were averaged from measurements taken at different segments of the SC in the MRI scans. Subcutaneous fat and muscle layers were also designed using internal offsets from the skin. The thickness values for these layers were set at 0.293 mm for subcutaneous fat and 0.114 mm for muscle, according to the previous mouse skin structural study from Neutelings et al. [38]. All surface meshes of the designed tissues and layers are represented in Fig. 2.

Corrected surface meshes were imported into 3-MATIC module from MIMICS software (v16) (www.materialise.com/en/industrial/software /3-matic). Skin electrodes were designed and added in the model within 3-matic as rectangular-shaped electrodes, with surface dimensions of  $2\times 3~\text{mm}^2$  and  $4\times 6~\text{mm}^2$  for the anode and cathode, respectively, and 0.25 mm thickness representing the gel layer as interface between the skin and the electrode. The electrodes were placed

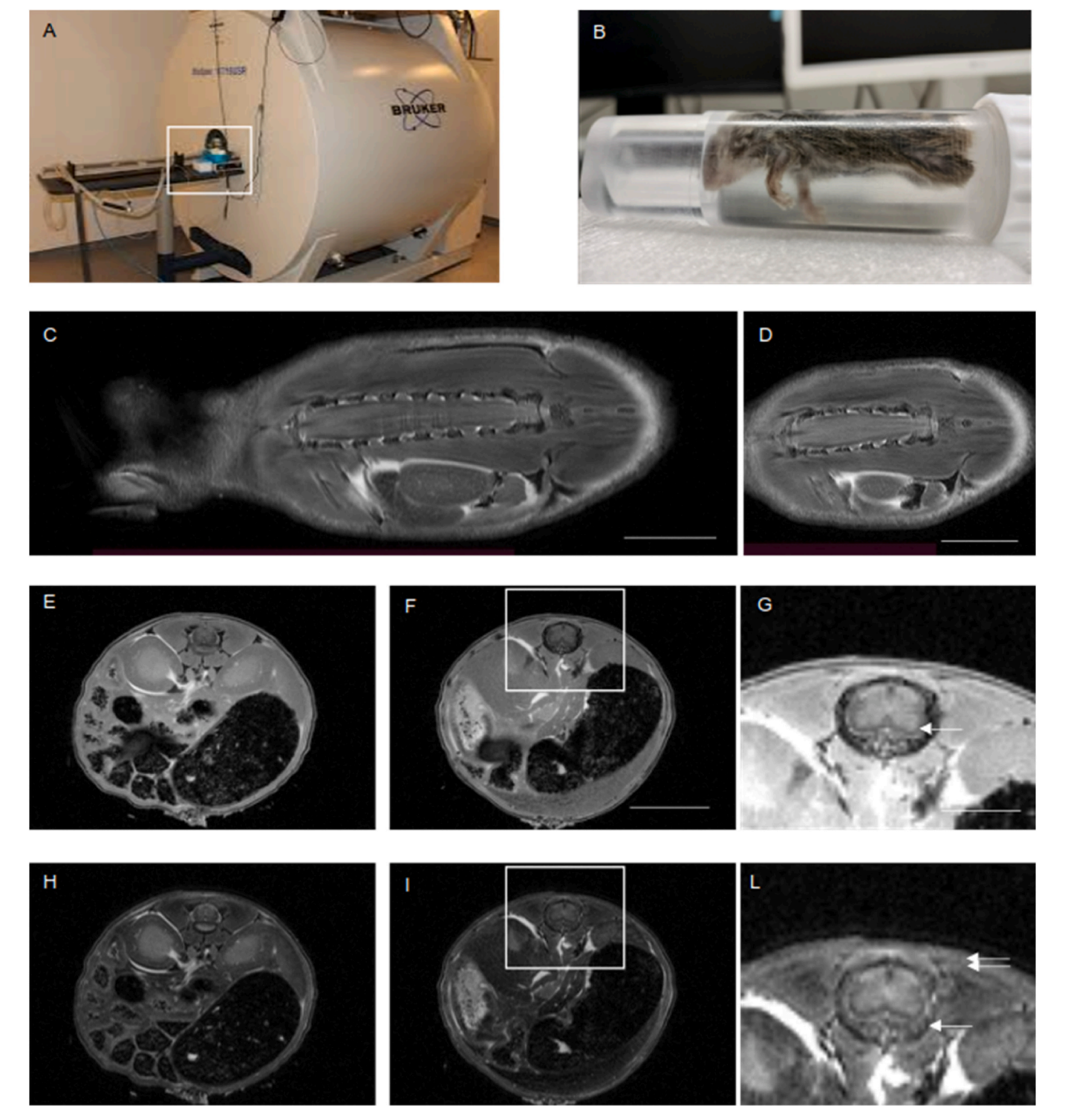


**Fig. 1. High-resolution ex-vivo MRI imaging for the generation of a whole-body anatomical reference dataset for modeling. A)** 11.7T small-animal MRI with dedicated holder (highlighted) used to record the dataset. **B)** Custom 3D-printed polycarbonate tube containing the PFA-perfusion-fixed mouse body immersed in perfluorinated hydrocarbon medium. The body floats naturally and it is kept in position by the shape of the tube. **C-D)** Coronal Images obtained at the level of the lumbar spinal cord highlighting the resolution of the spinal cord and the surrounding bone and soft tissue (c) and the distinction of longitudinal white-gray matter boundary (**D)**. Scale Bar 5 mm. **E-G)** Axial images obtained by FLASH at low-lumbar (L4-L5; **E)** and high lumbar (L1-L2; **F)** level. Inset of **F** is magnified in **G**, with increased contrast. Note the definition of the peri-spinal muscles and abdominal organs, and in the inset, the resolution of the cutaneous and subcutaneous structures as well as of the white-gray matter boundary (arrow, **G**). Scale Bar overview 5 mm, inset 2 mm. **H-L**) Axial images obtained by T2-RARE sequences (matched levels of **E-G**). Inset in I is magnified in L with increased contrast. Note the definition of the peri-spinal space and of the fat content of the bone (arrow, **L**) and of the subcutaneous tissue (double-arrow, **L**). Scale Bar overview 5 mm, inset 2 mm.

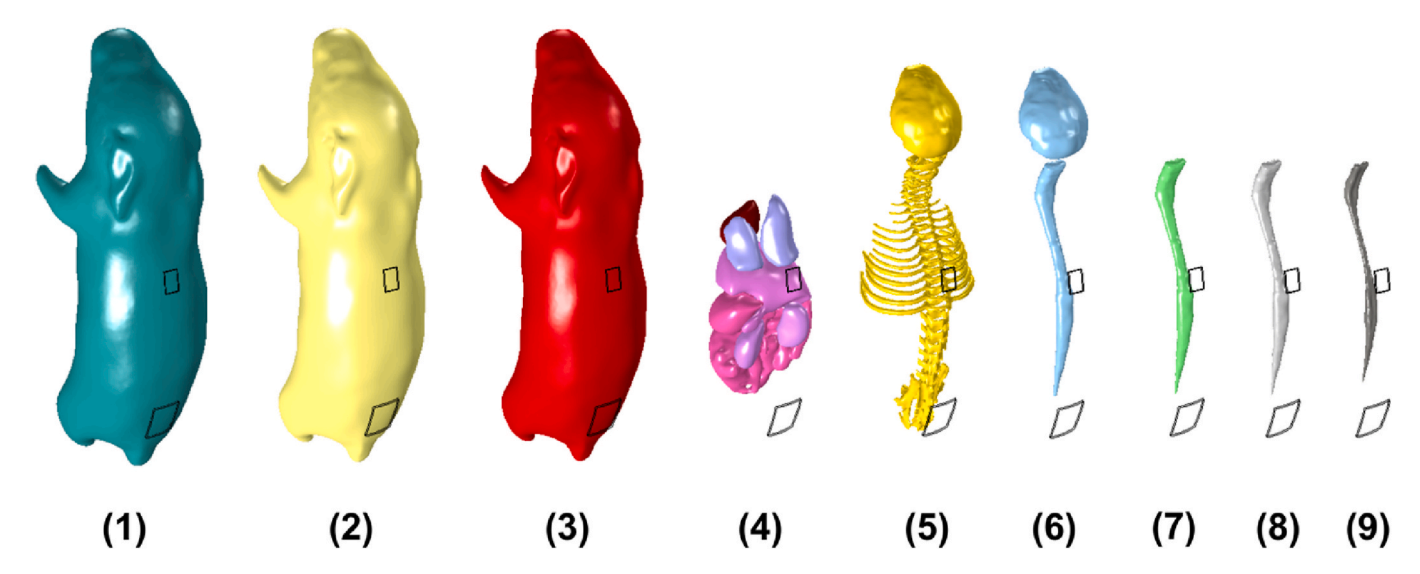


Fig. 2. Tissues surface meshes: skin (1); fat (2); muscle (3); heart, lungs, stomach, liver, spleen, pancreas, intestines (4); skull, vertebrae and intervertebral discs (5); brain and spinal dura (6); CSF (7); spinal-WM (8); spinal-GM (9).

in a rostral-caudal montage, with the anode over T10 spinous process (s. p.) and the cathode on S3 s.p. (Fig. 3).

Several surface correcting operations were applied: remeshing, filtering and smoothing sharp surfaces and edges. A non-manifold assembly of all surfaces and electrodes was obtained and a final volume mesh was generated, consisting of  $2.6 \times 10^6$  tetrahedral elements, adequate for applying in simulations using the finite-element method (FEM).

The surface and volume meshes of the full model with the electrodes was exported in a.mphtxt file format, compatible with COMSOL Multiphysics software (www.comsol.org) for FEM-based simulations.

### 2.2.2. Dielectric properties of biological tissues

A literature review on the electrical properties of biological tissues was conducted to compile a list of electrical conductivity values for DC currents, as shown in Table 1. We prioritized conductivity values derived from studies involving mice or other rodent species, such as rats or rabbits. When rodent-specific data were unavailable, we considered human estimates that integrate data across multiple species. It is important to note that there is significant variance in tissue electrical conductivities, both within and between species [39]. The measurements can be affected by factors such as current spreading through surrounding tissues, inhomogeneities at small scales, and potential errors from the electrode-tissue interface, which leads to a wide variability in reported low-frequency conductivities [40].

We specifically selected values from samples measured at body temperature ( $\sim$ 37 °C) and within the low-frequency range. In cases

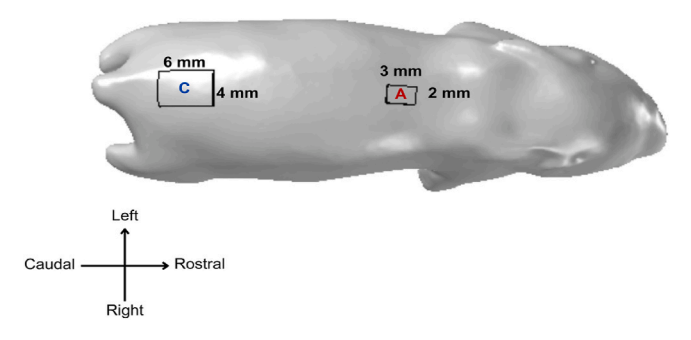


**Fig. 3.** Electrodes placement and surface dimensions on the mouse 3D computer model (A: anode; C: cathode). The orientation of the model is represented at the bottom left.

 Table 1

 Dielectric properties of biological tissues assumed in the mouse model.

Biological Tissue	Electric Conductivity (S/ m)	Literature Sources
Skin	0.435	Human [42]
Fat (in subcutaneous fat and fat surrounding spine)	0.040	Human [39]
Muscle	0.265	Rat - average between transversal
		and parallel values [43]
Bone (in skull, vertebrae, sacrum and ilium)	0.012	Rat [44]
Spinal WM	0.143	Human [45]
Spinal GM	0.300	Mouse - $\sigma = 0.316$ S/m measured
		at $f = 10^7$ Hz [46]; a lower value
0 1 . 10.1	1 700	was estimated using PLF trend
Cerebrospinal fluid	1.790	Human [47]
Dura Mater	0.060	Human [48]
Brain	0.284	Weighted average between WM
		(human [45]) and GM (mouse
		[46]), considering a WM:GM ratio of 90:10 [49]
Intervertebral Discs	0.200	Human [45]
Heart Discs	0.535	Human [45,50]
Lungs	0.046	Human [51]
Liver	0.123	Human [50]
Stomach	0.200	Human [45]
Intestines (small and	0.200	Human [45]
large)	5.200	
Pancreas	0.220	Human [39]
Spleen	0.100	Human [39]
Kidneys	0.100	Human [39]

where low-frequency data were not available, we performed a robust estimation based on the Power-Law Function trend [41] to estimate the most accurate values.

### 2.2.3. Computational simulations and model validation

The EF induced in the SC and surrounding tissues within the SOD1 mouse model were calculated using the AC/DC module of COMSOL Multiphysics software (www.comsol.com). A stationary study was run within the electric currents interface, adequate for low-frequency and DC currents. The Laplace equation for the electric potential  $(\phi)$ ,  $\nabla^2 \phi = 0$ , was solved by applying the finite element method (FEM) across each tissue and electrode domain. Boundary conditions were applied based

on the guidelines from Miranda et al. [52], which included:

- Continuity of the normal component of the current density at all interior boundaries;
- 2. Electric insulation at the external boundaries;
- 3. Electrode top surfaces were modeled as isopotential surfaces.

The potential difference between the anode and cathode was adjusted using COMSOL's floating potential boundary condition. This adjustment was made to maintain injected current constant through the electrodes. The electric field  $(\vec{E})$  was computed at all mesh element nodes by taking the gradient of the electric potential  $(\phi)$ , where  $\vec{E} = -\nabla \phi$ . All tissues were considered as purely resistive, with a relative permittivity  $(\epsilon_r)$  of 1 across all model domains, according to the quasistatic approximation, valid for DC currents [52,53]. The electric conductivity value of gel was obtained through a weighted average between four parts of Signa Gel (www.parkerlabs.com/products/signagel-electro de-gel/;  $\sigma = 4.000$  S/m) and one part of water ( $\sigma = 5.500$ x10 $^{-6}$  S/m; value obtained from COMSOL materials library), resulting in an effective gel conductivity of  $\sigma = 3.200$  S/m. This was done to reproduce more accurately the properties of the gel mixture used in the *in vivo* experimental setting.

Simulations and 3D modeling tasks were performed on a computer equipped with an NVIDIA RTX 2000 Ada Generation laptop GPU, 24 GB of total memory and a 13th Gen Intel® Core™ i7-13800H processor at 2.50 GHz. The system also had 32 GB of installed RAM, and a 64-bit operating system. Two values of injected currents were simulated - 10  $\mu A$  and 100  $\mu A$  - with a solution time of approximately 2 min and 3.8  $\times$   $10^6$  degrees of freedom.

Simulation results were exported from COMSOL and analyzed using Python scripts, employing the NumPy and Matplotlib libraries. The EF along the z-axis is calculated by averaging the EF magnitudes within a defined range around each z-coordinate. For each position z\_current, the code sums the EF values from electric\_field\_norms where the corresponding z-coordinates from z\_array fall within the range (z\_current delta z, z current + delta z), with delta z = 0.1 mm. The average EF is then computed by dividing the sum by the number of points within this range. If no points are found in the range, the EF is set to zero. This process is repeated for each slice along the z-axis, with the results stored in Av E norm. Various statistical metrics were then calculated, including mean, standard deviation, maximum, minimum, as well as the 95th and 99th percentiles of the average EF. These computational results were then compared with corresponding in vivo experimental findings to validate the model's accuracy. Comparison between simulation and experimental measures was performed by computing a computationalto-experimental ratio (RCE), along dorsal, intermediate, and ventral regions of the spinal GM right horn:

$$RCE = \frac{EF_{comp}}{EF_{exp}}$$
 (2.1)

where 
$$\underline{EF_{exp}} = \frac{\left| EF_{exp,anodal} \right| + \left| EF_{exp,cathodal} \right|}{2}$$
 (2.2)

Where  $EF_{comp}$  represents the value predicted by the *in silico* model,  $EF_{exp,anodal}$  and  $EF_{exp,cathodal}$  are the EF values determined experimentally during anodal and cathodal tsDCS, respectively.

### 2.3. In vivo electrophysiological measurement of the potential gradient

### 2.3.1. Animals

To validate the computational model of the DC spread, 6 B6SJL-Tg (SOD1\*G93A)1Gur/J mice bred at the Wielkopolska Center of Advanced Technologies at the Adam Mickiewicz University (Poznań, Poland) were used. Animals were housed two per cage at the Poznań University of

Physical Education Animal Facility (Poznań, Poland) with unlimited access to food and water. A reversed 12h/12h light-dark cycle was set in the room, and the humidity was maintained at 55  $\pm$  10 %, and the temperature at 22  $\pm$  2 °C. Electrophysiological experiments were conducted on male weighting 24.8  $\pm$  4.13g, and showing no ALS-related motor symptoms. All procedures were conducted with the approval of the Local Ethics Committee (approval number 15/2024), and all authors had the necessary permits for working with laboratory animals and were appropriately trained in all experimental procedures.

### 2.3.2. Surgery

The in vivo electrophysiological verification of the computational model was based on the procedures previously described in Ref. [19]. First atropine (0.20 mg/kg; Polfa, Poland) and methylprednisolone (0.05 Solu-Medrol; Pfizer, Poland) mix was injected subcutaneously to prevent salivation and edema, respectively. 15 min later intraperitoneal injection of a drug cocktail containing fentanyl (6.25 µg/ml; Polfa, Poland), midazolam (2.5 mg/mL; Polfa, Poland), and medetomidine (0.125/ml; Cp-Pharma, Poland) at a dose of 10 mL/kg body weight was made to anesthetize the animal. The anesthesia depth was assessed by the lack of the hind limb withdrawal reflex, which typically appears 5 min post-injection. Two electrocardiogram (ECG) needles were inserted subcutaneously to monitor the heart rate. The internal temperature was maintained at 37 °C by an infrared heating lamp and an electric blanket (TCAT-2DF; Physiltemp, USA). The tracheotomy was performed to artificially ventilate the animal with pure oxygen (SAR-1000 ventilator; CWE, USA), with parameters adjusted to maintain the end-tidal CO2 level at around 4 % (MicroCapstar; CWE, USA). Both external jugular veins were catheterized to deliver additional doses of anesthetic mix at 1.7 mL/kg body weight every 25 min. A physiological buffer (4 % glucose solution containing 1 % NaHCO3 and 14 % gelatine; Tetraspan; Braun, Poland) was administered through the second vein at 60  $\mu$ L/h to maintain mouse physiological balance. For electrical stimulation, the tibialis nerve was prepared by dissecting it from surrounding tissues and removing common peroneal and sural nerves. To immobilize the spinal column, two pairs of horizontal bars (Cunningham Spinal Adaptor; Stoelting, USA) were fixed at the Th12 and L2 vertebrae. Afterward, laminectomy was made to expose the L2 - L4 spinal cord segments (SS), from which the dura mater was removed to allow the microelectrode to be inserted into the spinal cord. The exposed tissues were covered with mineral oil.

### 2.3.3. tsDCS electrode arrangement and stimulation

Two silver rectangular electrodes were placed in a rostrocaudal arrangement on the skin on the back of the animal. Prior to electrode placement, the fur at the electrode location was shaved and electroconductive gel (Signa Gel; Parker Laboratories, USA) diluted 4/1 in tap water was applied to the skin to facilitate electrode contact. The rostral electrode, measuring  $2x3x0.25~\rm mm^3$  was placed on the skin above the Th10 vertebra. The second electrode,  $4x6x0.25~\rm mm^3$ , was positioned on the skin  $\sim\!\!21~\rm mm$  caudally, over the sacrum (Fig. 4. A). The rostral electrode polarity determined the tsDCS type, i.e. anodal tsDCS was applied when the rostral electrode had positive polarity, and cathodal tsDCS when it had negative polarity.

### 2.3.4. Recordings

Voltage deflection evoked by tsDCS was measured with glass microelectrodes with a tip of diameter 1–2  $\mu m$  and impedance of 10–15  $M\Omega$ , filled with 3M K-acetate solution. Extracellular recordings of the electric potential were made with an Axoclamp 900A amplifier (Molecular Devices, USA), connected to a Power1401 interface (CED, UK), operated by Spike2 software (CED, UK). The amplifier system was used in a bridge recording mode to minimize noise. All recording electrodes were compensated for electrode resistance, capacitance, and electrical offset. The measurements were made in three different zones of the spinal cord according to the tsDCS electrode placement. First voltage

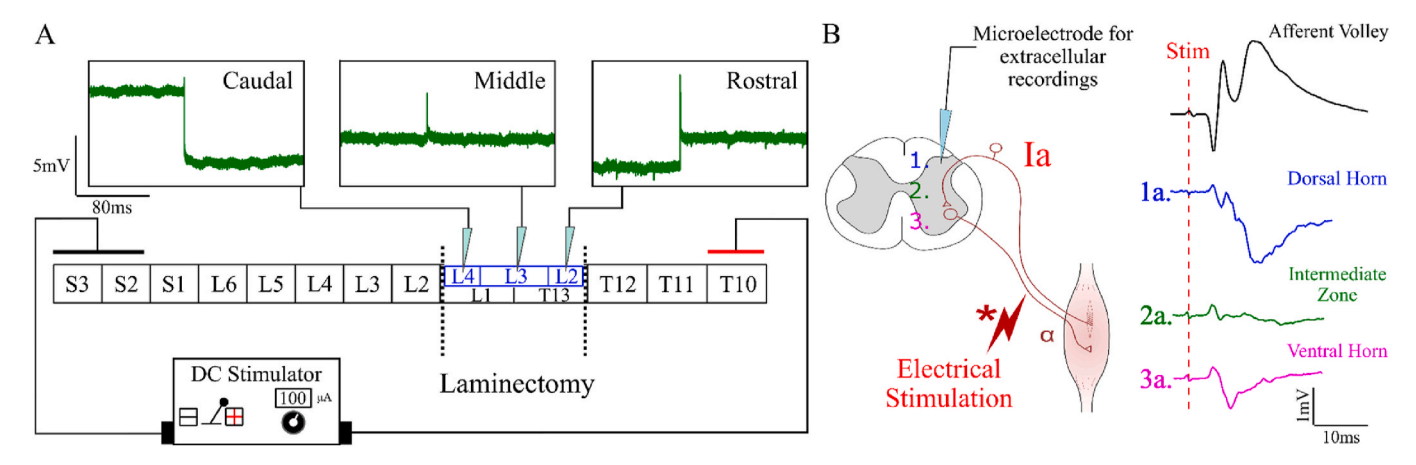


Fig. 4. tsDCS electrode arrangement and recording depths. (A) Location of tsDCS electrode in relation to the vertebrae, and spinal cord segments. "Caudal", "Middle", and "Rostral" indicate the zones of the voltage deflection measurements in reference to the rostral ("active") electrode. Black rectangles indicate vertebrae, while blue rectangles indicate the spinal cord segments. Green traces show examples of changes in voltage after switching ON anodal tsDCS of 100 μA current intensity in each recording zone. (B) Depths of the voltage deflection measurements in the dorsal horn (1), intermediate zone (2), and ventral horn (3), as identified by field potentials evoked by peripheral nerve stimulation (1a, 2a, 3a for dorsal horn, intermediate zone and ventral horn field potentials respectively). The top trace represents the afferent volley recorded from the surface of the dorsal spinal cord.

deflection was measured closest to the rostral electrode (L2 SS) then closest to the caudal electrode (L4 SS), and finally at the midpoint between previous recordings (L3 SS), as shown in Fig. 4. A. Measurements were also made at three depths, namely in the dorsal horn ( $\sim$ 300  $\mu$ m below the spinal cord surface), in the intermediate zone ( $\sim$ 600  $\mu$ m), and in the ventral horn ( $\sim$ 1200  $\mu$ m) of the spinal cord gray matter (Fig. 4. B).

The location of the microelectrode in the dorsal and ventral horns was confirmed by observing orthodromic or antidromic field potentials, respectively, evoked by electrical stimulation of sensory and motor fibers in the peripheral nerve, as shown in Fig. 4. B (modified from Jankowiak et al. [14]). The intermediate zone was defined as a depth between the dorsal and ventral horn, where no field potentials were observed.

After reaching each location, the recorded potential was zeroed against the reference electrode placed in the back muscles, and then a 15-min control recording of voltage was performed to ensure no "drift" in the recording. Afterward, the tsDCS was switched on, and the voltage deflection from the baseline was recorded simultaneously for another 15 min. Recordings were made for both anodal and cathodal polarization and current intensities of 10  $\mu A$  and 100  $\mu A$ . At the end of the experiment, a verification of the recording site was performed to ensure proper identification of spinal segments. To this end, we have identified the L2-L4 spinal nerves as they exit the spinal canal below the L2-L4 vertebrae through the intervertebral foramen. Then the dorsal branch of the nerve was dissected rostrally to the level where it enters the dorsal horn (Fig. 5). For all *in vivo* experiments the identified spinal segments matched the designated recording sites.

### 2.3.5. Statistics

The electrophysiological data was analyzed using R-Studio 2024.04.02 (Posit Software, PBC) with appropriate libraries. The Shapiro-Wilk test was used to test the normality of data distribution. As all the data met the normal distribution criteria, parametric tests were used to further analyze the data. All plots were created using the "ggplot2" package [54], and the Pearson correlation coefficient was calculated from built-in RStudio functions, to estimate the correlation between the voltage deflection and the distance to the active tsDCS electrode. The significance level for both the Shapiro-Wilk test and the correlations was set at p < 0.05.

### 3. Results

### 3.1. Description of MRI datasets

In order to provide a realistic anatomical model for the computation analysis of the current propagation, we elected to use ultra-high-field exvivo MRI acquisition in a perfluorinated hydrocarbon medium (Fluorinert). The use of MRI supported the differentiation of anatomical structures with high contrast and the ultra-high-field and the long acquisition time (only possible for ex-vivo samples, 18-24h) enabled an exquisite spatial resolution across the body. The signal-to-noise ratio was further improved by the use of the Fluorinert acquisition medium: being devoid of hydrogen atoms, this perfluorinated agent does not produce any signal in <sup>1</sup>H-MRI and did not generate susceptibility artifacts within the tissue [55]. Overall, this pipeline resulted in a 50  $\mu m$ (XY) resolution, sufficient to resolve not only the boundaries of organs but also to isolate different layers of subcutaneous structures as well as to distinguish white and gray matter through the spinal cord length. The MRI dataset included the head and the body of the mouse; in order to reduce aliasing artifacts, the distal part of the limbs was not included in the imaging field of view, and tail was removed in order to fit the body within the plastic holder. Three distinct mice were imaged, generating a multiplexed dataset enabling the reconstruction of the whole-body anatomy (example for one mouse in Fig. 1).

## 3.2. Prediction of tsDCS-induced effects in the realistic mouse computational model

The modeling study was performed using the mouse model obtained from one of the three mice MRI datasets described in 3.1., and using methods previously described in section 2.2. The isotropic electrical properties of tissues were assigned as indicated in section 2.2.2 and the EF volume distribution was calculated using the FEM as in section 2.2.3, for two values of injected current, 10  $\mu A$  and 100  $\mu A$ .

The EF magnitude in the spinal GM presents maximum values of 0.57 V/m for I = 10  $\mu$ A, and 5.7 V/m for I = 100  $\mu$ A. These maximum values are located at the level of T12 and T13 s.p., near the anode caudal extremity. As expected for purely resistive conditions, the EF magnitude is proportional to I: it is 10 times larger for I = 100  $\mu$ A when compared to the values predicted for I = 10  $\mu$ A, thus the spatial distribution of the EF presents the same features (Fig. 6). Fig. 7 shows the volume-weighted average of the EF magnitude profile along 1 mm-thick slices along the z direction for 10  $\mu$ A. Analogously, the same distribution profile is

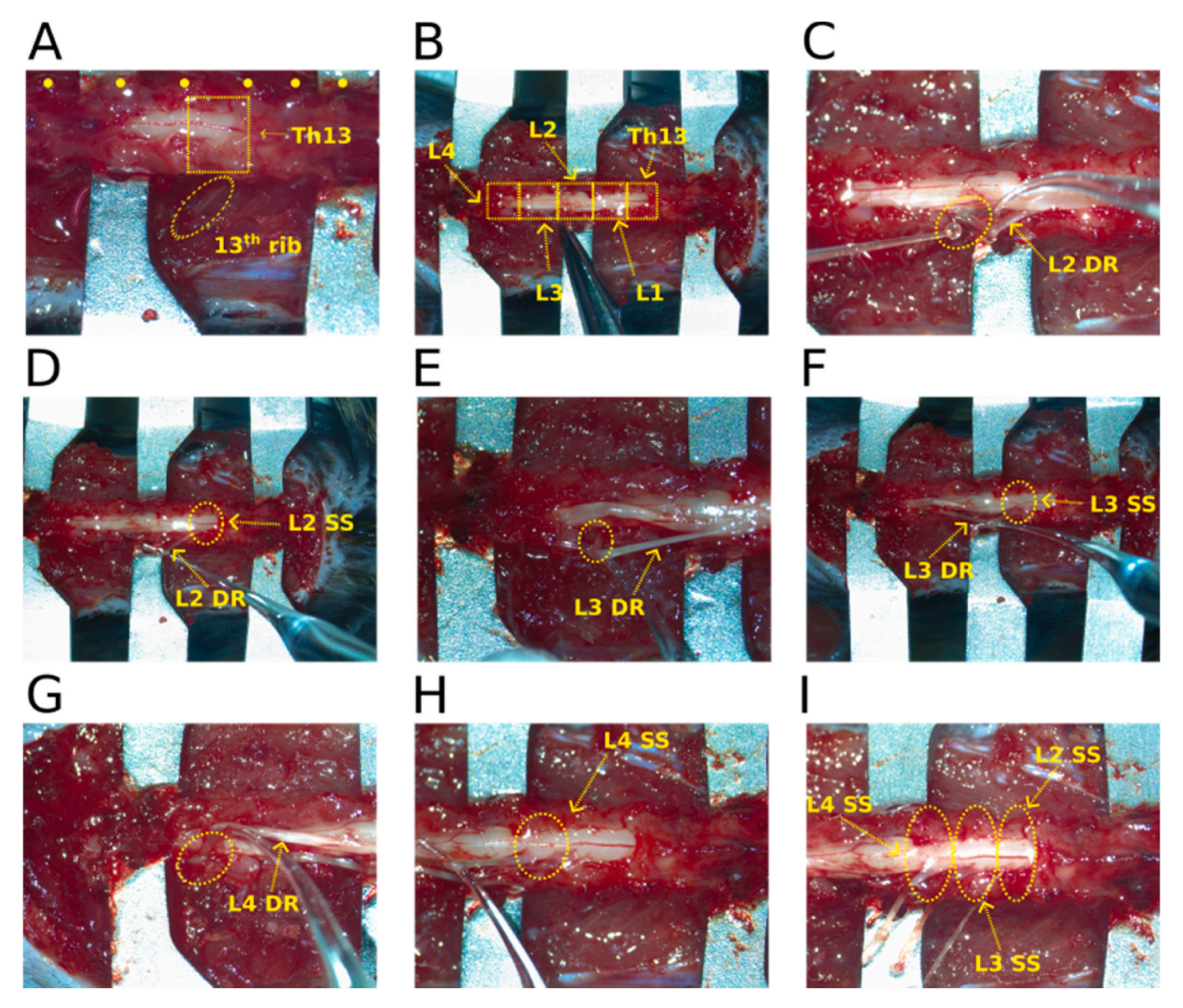


**Fig. 5. Identification of spinal segments. A)** Following laminectomy and soft tissue removal, the 13th rib is identified as the last rib connecting to the rostral part of the 13th vertebrae. The yellow dots indicate the transverse processes of the Th11 - L3 vertebrae. B) Laminectomy is expanded between Th 13 and L4 vertebrae. Notice that for demonstration purposes an extra pair of spinal clamps is used at L5 and the spinal clamps used to stabilize the spinal column at Th12 are moved rostral. The individual vertebrae are marked with yellow squares C) L2 dorsal root (DR) is identified as a bundle of nerve fibers exiting the spinal canal through the L2 intervertebral foramen (yellow circle) between L2 and L3 D) The L2 dorsal root is then dissected rostrally up to it's entry to the spinal cord. This marks the L2 spinal segment (SS). E-H) Similar to C-D, but identifying the L3 and L4 SS. I) L2-L4 DR are cut distally and retracted and the L2-L4 spinal segments are marked.

obtained for 100  $\mu A.$  A single large peak is reached below the anode location, for both simulations, encompassing the vertebral levels T10 to T13. Current intensity only changes the EF magnitude and not its spatial pattern.

Fig. 8 presents EF magnitude in axial slices taken on the section where experimental measurements were taken, specifically in L2 to L4 SS, for applied currents of 10  $\mu$ A and 100  $\mu$ A. The same patterns were seen for both current intensity values in each slice, with changes only in EF magnitude, for the same reasons stated above (EF linearly proportional to I). Tables 2 and 3 summarize the maximum and minimum EF values observed at each slice, along with the corresponding SS and vertebrae locations. Notably, the EF values decrease consistently along the z-axis, or more caudally along the SC, which goes in line with the higher values measured under the anode region, near the T10 vertebra.

### 3.3. Experimental measurements

In vivo electrophysiological experiments were performed to assess the deflection of the voltage induced by tsDCS. Figs. 9 and 10 show the relationship between the distance from the rostral ("active") electrode to the recording zone, and the deflection of the voltage for both polarization types, at current intensities of 10  $\mu A$ , and 100  $\mu A$ . The linear fit was estimated through the Orthogonal Distance Regression. This method accounts for observational error on both independent and dependent variables [56]. In this case the uncertainty associated with the distance to the anode measurements is  $\pm 0.25$  mm, and the uncertainty of the voltage deflections measurements falls within  $\pm 0.15$  mV.

During anodal polarization, a strong depolarization (positive deflection) was observed in the vicinity of the rostral electrode at every depth of the recording. This effect diminishes with increasing distance from the electrode and eventually transitions into a negative shift (Fig. 9A–C).

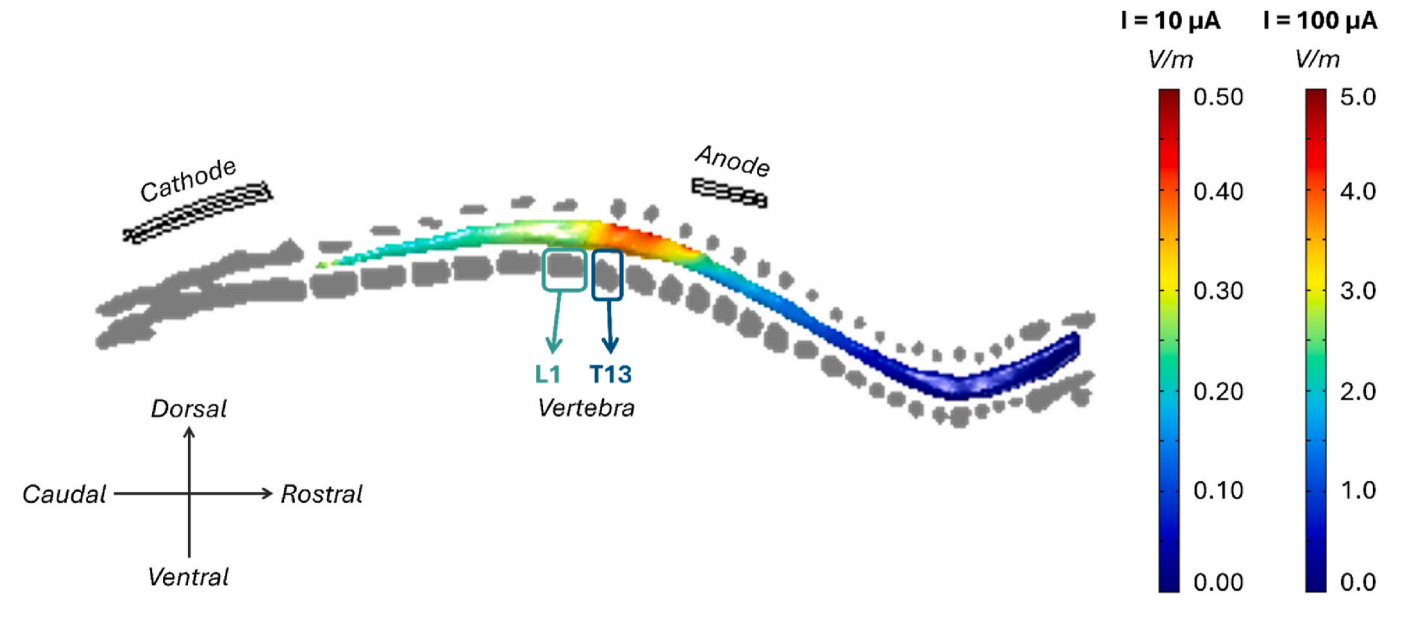


Fig. 6. Volume distribution of the EF magnitude in spinal GM predicted for current intensities of 10 and 100  $\mu$ A; (sagittal view). Vertebrae positions are presented by a sagittal slice in gray to illustrate the anatomical locations relative to the spinal GM. A color scale for the EF magnitude is represented at the right and the orientation of the spinal cord at the bottom left.

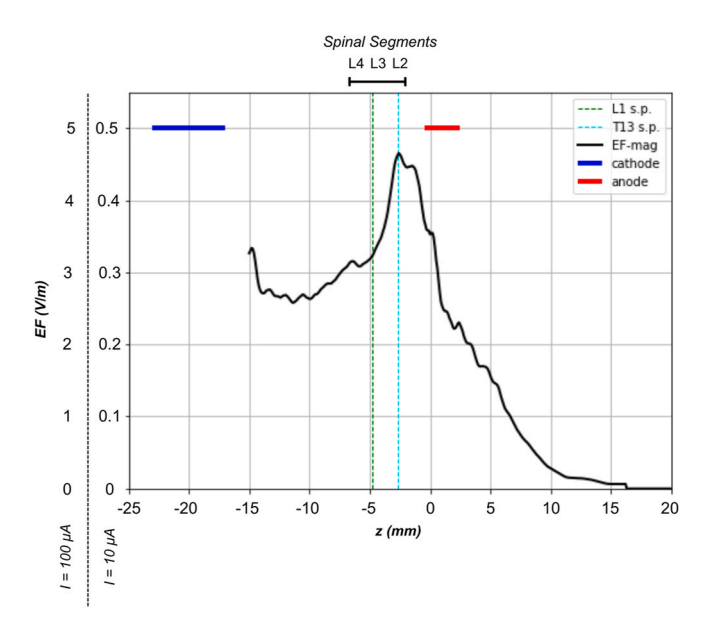


Fig. 7. Average EF magnitude distribution along the z direction (volume-weighted in 1 mm-thick slices) in the spinal-GM (I = 10 and 100  $\mu$ A). EF-mag: EF magnitude; s.p.: spinal vertebral processes.

This voltage change was significantly and negatively correlated with the distance from the active (rostral) electrode in the dorsal horn (r(13) =  $-0.91,\,p<0.001$ ), intermediate zone (r(13) =  $-0.70,\,p=0.004$ ), and ventral horn (r(13) =  $-0.84,\,p<0.001$ ). Conversely, during cathodal polarization, the voltage deflection exhibited a significant positive correlation with increasing distance, with values of r(13) =  $0.75,\,p=0.001;\,r(13)=0.71,\,p=0.003;$  and r(13) =  $0.83,\,p<0.001$  for the dorsal horn, intermediate zone, and ventral horn, respectively (Fig. 9D–F).

The same dependencies were observed for 100  $\mu A$  current intensity as shown in Fig. 10. Again, the voltage shift was significantly and negatively correlated with increasing distance from the active electrode in the dorsal horn (r(13) = -0.88, p < 0.001), intermediate zone (r(13) = -0.91, p < 0.001) and ventral horn (r(13) = -0.88, p < 0.001) for anodal tsDCS (Fig. 10A–C). Similarly to 10  $\mu A$ , during cathodal

polarization, a significant and positive correlation of voltage deflection was observed with r(13) = 0.89, p < 0.001; r(13) = 0.89, p < 0.001; r (13) = 0.87, p < 0.001 for dorsal horn, intermediate zone, and ventral horn, respectively (Fig. 10D–F).

The average voltage deflection  $\pm$  SD, for each recording depth and zone, tsDCS type, and current intensity are shown in Table 3.

### 3.4. Comparing computational and experimental results

As previously described in section 2.1, computational and experimental results were compared through the calculation of the ratio between predicted and estimated EF values (equation (2.1)). To ensure a meaningful comparison, the computational measurements predictions of EF were aligned as closely as possible with the experimental protocol. Hence, the mean, minimum, maximum, 95th and 99th percentiles, median, and standard deviation were calculated between L2 and L4 SS, corresponding to T13 and L1 vertebrae (-5.5 < z < -2.4 mm), at the GM right horn (-0.7 < x < 0.3 mm) under the following conditions:

- For dorsal region (-9.4 < y < -8.7 mm);
- For intermediate region (-8.7 < y < -8.4) mm;
- ullet For ventral region: (-8.4 < y < -7.8) mm.

For reference, the coordinate system is defined as follows: x denotes the left–right axis (with negative values corresponding to the left side), y the dorsal–ventral axis (with negative values oriented ventrally), and z the rostral–caudal axis (with negative values directed caudally).

Comparison of modeling predictions with the experimental results following the procedure above are summarized in Tables 4 and 5, for 10  $\mu A$  and 100  $\mu A$ , respectively.

Only the EF absolute values predicted by simulations are presented. EF values for the simulations were determined considering anodal stimulation (anode over T10 s.p.). In this case, the EF is rostral-caudal oriented. For cathodal stimulation, the EF will only change sign, being caudal-rostrally oriented. This is in line with the small differences measured experimentally: values of the potential gradient (-EF, according to  $\vec{E}=-\nabla\phi$ ) during anodal and cathodal stimulation polarities only differ by 0.01–0.05 V/m (see Figs. 9 and 10).

The computational simulations produced EF values that were within

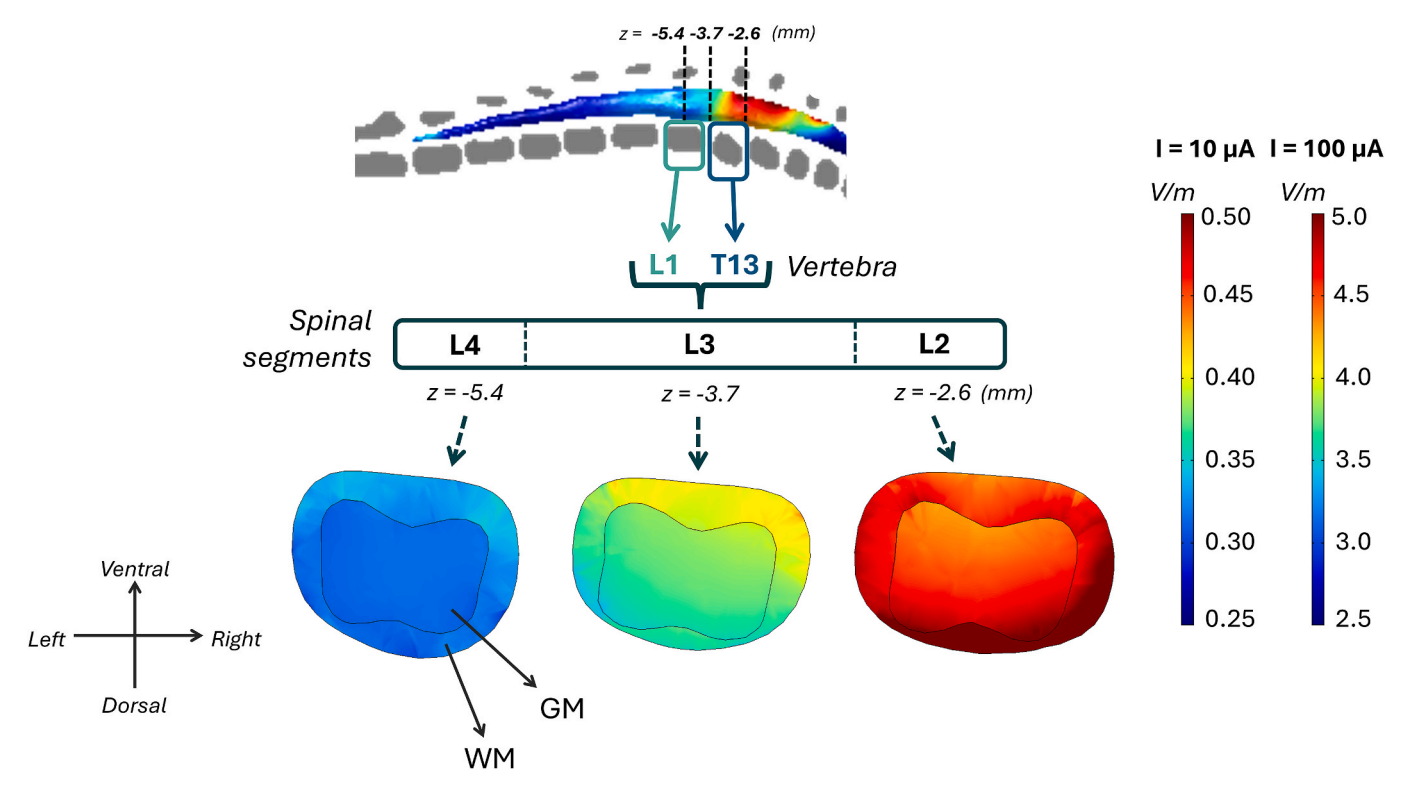


Fig. 8. From left to right (caudal to rostral): EF magnitude in axial slices taken in SS L4 to L2 (between L1 and T13 vertebrae) at current intensities of  $10 \mu A$  and  $100 \mu A$ . The top diagram shows the location of each slice. A color scale for the EF magnitude is represented at the right and the orientation of the axial slices at the bottom left.

Table 2 EF maximum and minimum values at axial slices taken in SS L4 to L2, predicted for I  $=10~\mu A$  and I  $=100~\mu A$ .

		z = -5.4 mm	z = -3.7 mm	z = -2.6 mm	
SS		L4	L3	L2	
Minimum GM (V/	$I = 10 \ \mu A$	0.306	0.339	0.427	
m)	$\begin{array}{l} I=100 \\ \mu A \end{array}$	3.06	3.39	4.27	
Maximum GM (V/	$I = 10 \mu A$	0.322	0.398	0.508	
m)	$I=100$ $\mu A$	3.22	3.98	5.08	
Minimum WM (V/	$I = 10 \mu A$	0.293	0.340	0.431	
m)	$I=100$ $\mu A$	2.93	3.40	4.31	
Maximum WM (V/	$I = 10 \ \mu A$	0.351	0.437	0.593	
m)	$\begin{array}{l} I=100 \\ \mu A \end{array}$	3.51	4.37	5.93	

the same order of magnitude as the experimental results. However, the simulated EF values were consistently around 2 to 4 times larger than the experimental values at currents of 10  $\mu A$  and 100  $\mu A$ . As anticipated, the EF values generated at a current of 100  $\mu A$  were 10 times greater than those at 10  $\mu A$ , reflecting the low-frequency and DC study conditions.

To assess if the experimental data follow the linear DC conditions, we calculated the ratio between estimated EF values (slope of the linear orthogonal distance regression) for 100  $\mu A$  and 10  $\mu A$  (equation (3.1)). The values are presented in Table 6.

Ratio 
$$(EF_{exp}) = \frac{EF_{exp,100 \mu A}}{EF_{exp,10 \mu A}}$$
 (3.1)

Except for the Anodal, Dorsal condition, the expected linear trend by a factor of 10 (from the computational prediction and from the quasi-

static approximation valid for DC currents) is within the corresponding intervals of these ratios. However, we observe more distinct values for both Anodal, Dorsal and Cathodal, Ventral Ratios, which may reflect a systematic uncertainty on those experiments.

### 4. Discussion

This study is the first to our knowledge to combine modeling predictions of the electric field induced by tsDCS in mice with experimental measurements made *in vivo* during real stimulation. An MRI-based realistic mouse body model anatomically similar to the SOD1 mouse was generated, with a clear definition of vertebrae, spinal tissues, including dura, WM, and GM, and surrounding tissues, such as bone, muscles, lungs, heart and viscera. This hybrid *in silico - in vivo* methodology allowed us to ascertain the validity of the computational model and identify issues to improve its predictive accuracy.

### 4.1. Computational versus experimental results

The electric field spatial patterns match in orientation and variation along spinal cord segments between the stimulating electrodes. However, we identified a systematic difference between the EF magnitude values measured and predicted, with computational values consistently 2 to 4 times larger (see Tables 5 and 6). A possible source for this consistent difference may arise from assumptions made regarding the conductivity values of tissues in the model. The most recent conductivity study referenced in our work is from 2005 [48], indicating that these values may be outdated. Additionally, we used human and different rodent conductivity values due to a lack of specific data for mice, which may not accurately represent murine tissues. For instance, we assumed muscle conductivity to be similar, though slightly lower, than GM conductivity, but this assumption may not be valid given the physiological differences between these two tissues [57,58].

Another possible source of inconsistency of predicted and measured

Table 3 Average voltage deflection from the baseline ( $\pm$ SD) in the dorsal horns, intermediate zone and ventral horns gray matter during anodal and cathodal tsDCS of 10 and 100  $\mu$ A. Measurements were taken at the rostral, middle and caudal recording zones. Positive voltage deflection (depolarization) is marked in green, while negative voltage deflection (hyperpolarization) is marked in red. Data from n=6 mice.

Depth of the recording	TsDCS type	Current intensity	Average deflection rostral (mV)	Average deflection middle (mV)	Average deflection caudal (mV)
Dorsal		10 µA	0.54±0.21	-0.13±0.22	-0.72±0.20
Intermediate	Anodal		0.41±0.37	-0.12±0.38	-0.62±0.34
Ventral			0.27±0.25	-0.08±0.15	-0.69±0.34
Dorsal			-0.19±0.37	0.20±0.25	0.66±0.30
Intermediate	Cathodal		-0.47±0.33	0.20±0.36	0.56±0.13
Ventral			-0.20±0.23	0.21±0.22	0.60±0.28
Dorsal			0.74±1.78	-1.88±2.41	-5.61±1.89
Intermediate	Anodal	100 µA	0.79±1.61	-1.64±1.88	-6.13±1.68
Ventral			0.86±1.27	-1.67±1.83	-6.43±1.64
Dorsal	Cathodal		-0.92±1.81	1.45±1.93	5.44±1.58
Intermediate			-1.78±0.94	1.34±1.26	5.87±1.81
Ventral			-0.81±1.06	1.01±0.70	6.51±1.91

EF magnitudes is the uncertainty of experimental measures, as evidenced in Table 6. Specifically, we observed that the expected linear trend from the DC condition is not entirely present on the experimental data: The standard errors associated with the computed ratios (ranging from 1.0 to 2.6) confirm the variability in the experimental measurements. Both the distance to the active electrode and the voltage deflection measurements have uncertainties associated that will affect the EF estimation, as we confirm in the presented results.

Contributions of interindividual anatomy of the experimental set up mice may also contribute to the systematic difference between model and experimental data. The standard deviation of the average voltage deflection values in Table 4 can reach values as high as 1–4 times the average (maximum coefficient of variation of 3.9 in the dorsal region). Different anatomical size, thickness of tissues surrounding the spinal cord, protrusions of discs into the spinal canal, intervertebral space, are among several factors that can contribute the decrease the accuracy of computational models [29,59,60].

Another factor not fully replicated in the simulations is the surgical setup applied to measure the voltage gradient *in vivo*. First, surgical tools and components present in the experimental setup were not modeled, even though they could influence the current distribution and potentially affect the resulting EF. On the other hand, the impact of the surgical opening on EF magnitude and patterns was specifically assessed as a potential source of discrepancy between simulation and experimental results. We simulated this opening in the model for I = 10  $\mu A$ . Results showed minimal difference in EF values ( $\sim\!0.01~V/m$  or  $\sim\!3$ %) between the model with the surgical opening and the default model. Moreover, the surgical opening model took significantly longer to run (20 min, about 10 times longer). Given the added complexity of handling conductivity tensors and the lack of substantial improvement in results, the

default model provided similar results with a simpler setup and faster simulation time. Additionally, most experiments with tsDCS in mice reproduce human settings as closely as possible, by measuring motor responses and evaluating changes due to the stimulation, without any opening at the spinal level. The similarity between predictions reported above ensures that the default model keeps the relation between predicted and measured EFs obtained, thus being adequate virtual bench to reproduce conditions of real tsDCS experiments.

### 4.2. Role of computational studies to plan experimental protocols

Computational modeling plays a crucial role in optimizing tsDCS protocols by predicting EF distributions and guiding experimental design. Despite discrepancies in EF magnitudes due to potential inaccuracies in conductivity values and experimental factors, the EF spatial patterns align well with experimental expectations, supporting the use of these models in refining experimental setups.

Previous studies highlight the importance of computational models in tsDCS research and experimental planning. Zareen et al. used an MRI + CT-based rat model to optimize cervical tsDCS after spinal cord injury, identifying the cervical enlargement as the region with the highest current density  $(0.7\ \text{A/cm}^2)\ [26].$  Their approach, combined with bilateral epidural theta burst stimulation, enhanced motor cortex responses and functional recovery. Similarly, Williams et al. applied computational models in cats to target corticospinal tracts, validating their predictions experimentally [25]. Both models are focused on optimization of current spread and density to the stimulation target, whereas our study aims to predict spatial distribution and geometric constraints related to the EF.

Our study builds on these approaches (realistic volume conductor

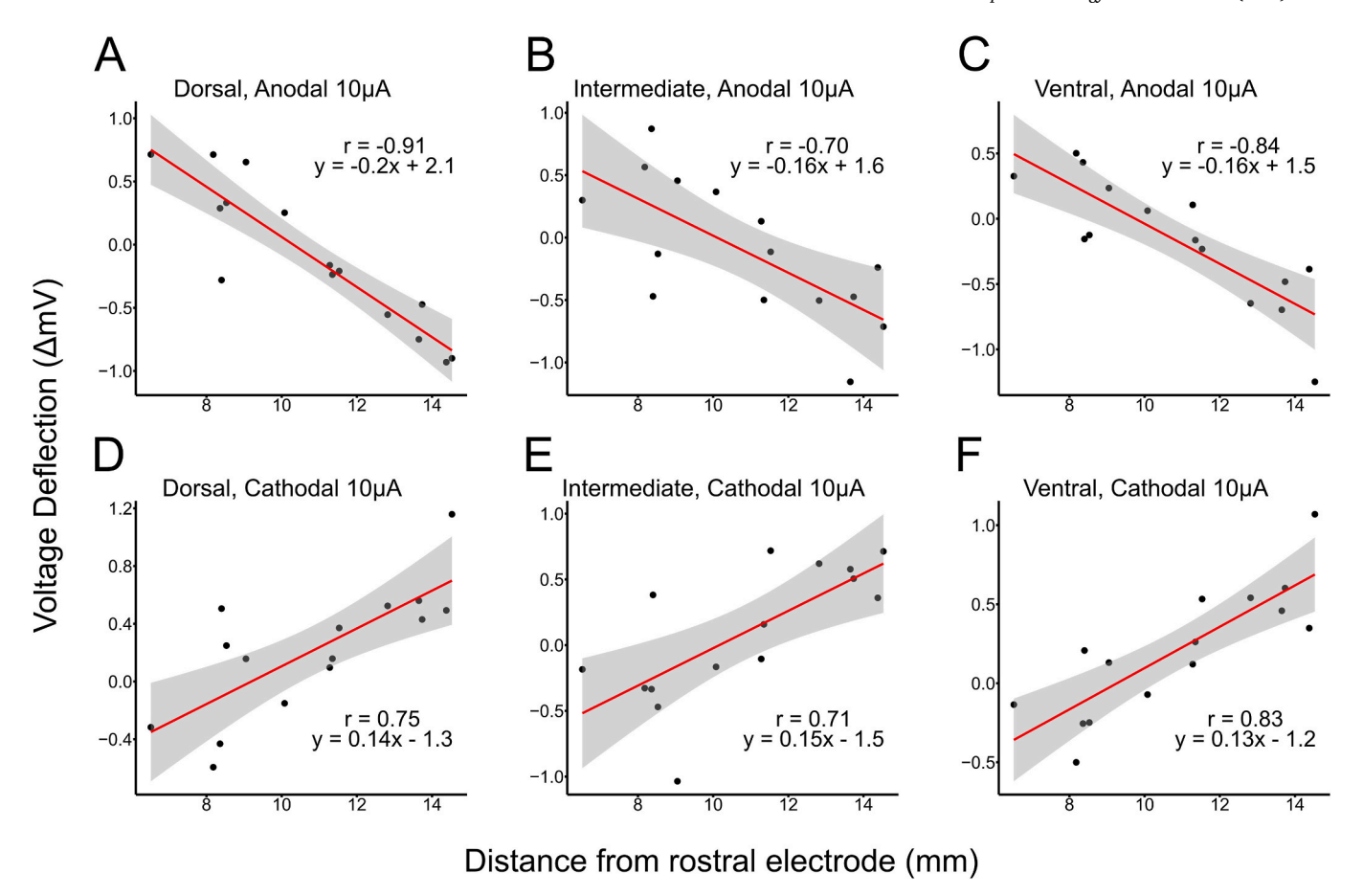


Fig. 9. Variation of voltage deflection with distance from the active electrode. Voltage deflection during anodal (A–C) and cathodal (D–F) tsDCS of  $10~\mu$ A stimulation intensity is plotted versus the distance from the active (rostral) electrode, for dorsal horn (A, D), intermediate zone (B, E) and ventral horn (C, F) gray matter recording depths. The experimental data was fitted to a linear fit function of the form y = mx + b, represented by a red line and indicated on the left, including the Pearson correlation coefficient (r). Gray areas represent the confidence interval which was set at 95 %. Notice a strong negative correlation for the anodal, and an opposite positive correlation for cathodal tsDCS effects. Data from n = 5 mice.

models based on medical imaging and FEA) but introduces key distinctions. In our knowledge, this is the first computational study of tsDCS on a small animal as the SOD1 mouse. In our 100  $\mu A$  simulation, the current density in the L2-L4 SS reached a maximum of 0.86 A/cm², with a 95th percentile of 0.75 A/cm² - similar to Ref. [26]. However, while previous studies focused on cervical and thoracic tsDCS, we target the lumbar spinal cord, where the current must pass through thicker fat and muscle layers, resulting in different EF and current distribution compared to cervical applications. Nonetheless, by simulating various current intensities and analyzing the EF spatial patterns alongside experimental results, our work shares the goal of improving tsDCS planning.

### 4.3. Lumbar tsDCS: human vs mouse models

While no *in silico* models of lumbar tsDCS in animals have been identified, previous modeling studies have investigated lumbar tsDCS application in humans. Comparing our mouse model with those studies provides insights into the translation of computational findings. Fernandes et al. demonstrated how different electrode montages can significantly affect EF pattern in a human computational model, influencing the modulation of both sensory and motor pathways [29]. Their model revealed EF values exceeding 0.15 V/m in the anterior and posterior horns of the spinal GM, indicating potential effects on both sensory and motor nuclei. Similarly, both our computational and experimental studies resulted in EF values larger than 0.15 V/m, however, it is not clear yet if this EF threshold - defined for human tissues

and for tDCS application [52,61] - translates into neuromodulatory effects on mice SC.

Pereira et al. combined computational modeling with experimental validation, finding that montages producing higher current density and EF magnitudes, particularly between the T8 and L2 spinal segments, led to significant physiological effects, such as an increase in the H-reflex amplitude following cathodal tsDCS [13].

The alignment between computational predictions and experimental outcomes in these human studies mirrors the approach taken in animal models. Our SOD1 mouse model aims to understand tsDCS effects on a more detailed level, with the aim that our results build confidence for the application of this therapy approach to humans with MNDs like ALS. The overall patterns observed in both animals and humans, such as the influence of electrode positioning and current intensity on EF, underscore the potential for computational models to guide experimental protocols and optimize translational clinical applications.

## 4.4. Relevance of a realistic model of a SOD1 mouse validated for tsDCS investigations

tsDCS alters spinal tracts and spinal circuit activity in humans [1,62], and modeling studies have identified the most effective electrode montage for providing the highest current densities in human applications [13,63]. However, the human models are impossible to verify because current techniques available to measure EF *in vivo* in humans will be harmful, limiting our understanding of the mechanisms behind tsDCS actions, especially with regard to the spatial distribution of the DC

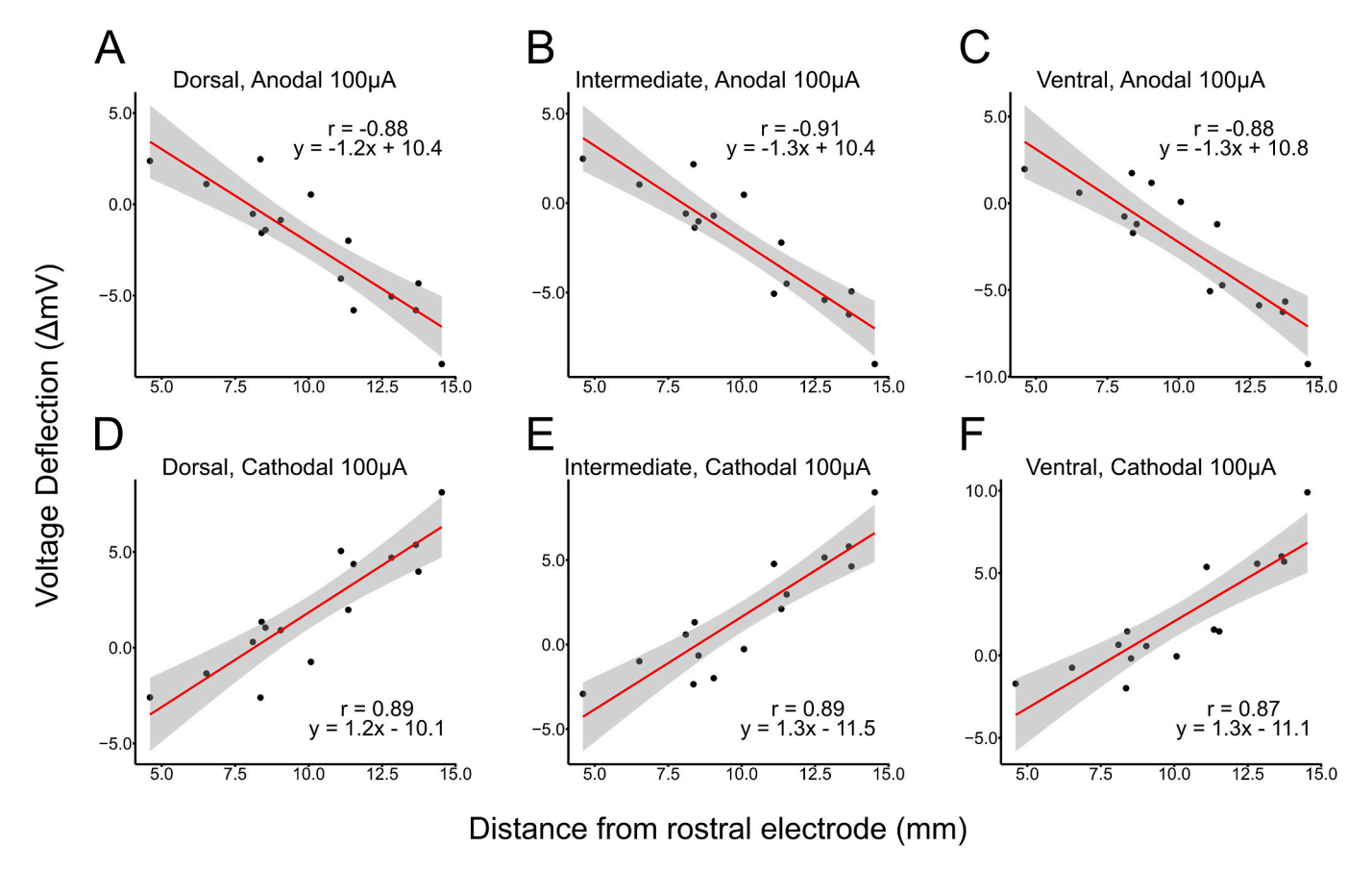


Fig. 10. Variation of voltage deflection with distance from the active electrode. Voltage deflection during anodal (A–C) and cathodal (D–F) tsDCS of 100  $\mu$ A stimulation intensity is plotted against the distance from the active (rostral) electrode, for dorsal horn (A, D), intermediate zone (B, E) and ventral horn (C, F) gray matter recording depths. The experimental data was fitted to a linear fit function of the form y = mx + b, represented by a red line and indicated on the left, including the Pearson correlation coefficient (r). Gray areas represent the confidence interval which was set at 95 %. Notice a strong negative correlation for the anodal, and an opposite positive correlation for cathodal tsDCS effects. Data from n = 5 mice.

Table 4 Comparison between EF magnitude values predicted and determined experimentally in the spinal GM for  $I=10~\mu A$ . Values of the potential gradient measured experimentally in the GM: voltage gradients in V/m are indicated for dorsal, intermediate and ventral right regions (slopes of linear regressions in Fig. 9). EF experimental value  $EF_{exp}$  was determined by equation (2.2) were determined for each region. Statistical metrics for EF values predicted by the model for dorsal, intermediate, and ventral right regions. Only the absolute values are presented, since these are equal for both polarities (EF orientation is rostral-caudal in anodal stimulation and the opposite in cathodal stimulation). RCE, the ratio of computational/experimental EF values, was determined with equation (2.1). StdDev: standard deviation.

Experimental data - voltage gra	dient in V/m (Slope of li	near fit)				
Voltage gradient (V/m)	Dorsal	StdDev	Intermediate	StdDev	Ventral	StdDev
EF <sub>exp,anodal</sub>	0.20	0.02	0.16	0.04	0.16	0.03
EF <sub>exp,cathodal</sub>	0.14	0.03	0.15	0.04	0.13	0.02
$\underline{EF}_{exp}$	0.17	0.02	0.15	0.03	0.15	0.02
Computational predictions - ele	ctric field in V/m					
EF magnitude (V/m)	Dorsal	RCE	Intermediate	RCE	Ventral	RCE
Mean	0.38	2.24	0.38	2.44	0.38	2.59
Minimum	0.30	1.80	0.31	1.99	0.30	2.07
Maximum	0.52	3.08	0.49	3.19	0.46	3.17
Percentile 95	0.50	2.97	0.48	3.12	0.45	3.07
Percentile 99	0.51	3.00	0.49	3.18	0.46	3.13
Median	0.36	2.10	0.35	2.25	0.38	2.61
StdDev	0.06	-	0.07	-	0.05	-

current and EF in the spinal cord. It is still not known whether the effects of tsDCS depend on the current density at the target side, the current polarity (anodal vs. cathodal) or the spatial orientation of neuronal compartments with respect to the induced electric field. In this study, we have for the first time created a realistic *in silico* model of tsDCS-induced

electric field in a mouse, and importantly we have validated it with *in vivo* measurements of the electric field using the DC voltage gradient along the lumbar spinal segments between the stimulating electrodes, with an innovative method not applied before to our knowledge. This was possible due to our state-of-the-art technique allowing intraspinal

Table 5

Comparison between EF magnitude values predicted and determined experimentally in the spinal GM for  $I=100~\mu A$ . Values of the potential gradient were measured experimentally in the GM: voltage gradients in V/m are indicated for dorsal, intermediate and ventral right regions (slopes of linear regressions in Fig. 10). EF experimental value  $EF_{exp}$  was determined by equation (2.2) for each region. Statistical metrics for EF values predicted by the model for dorsal, intermediate, and ventral right regions. Only the absolute values are presented, since these are equal for both polarities (EF orientation is rostral-caudal in anodal stimulation and the opposite in cathodal stimulation). RCE, the ratio of computational/experimental EF values, was determined with equation (2.1). StdDev: standard deviation.

Experimental data - voltage gradient in V/m (Slope of linear fit)						
Voltage gradient (V/m)	Dorsal	StdDev	Intermediate	StdDev	Ventral	StdDev
EF <sub>exp,anodal</sub>	1.24	0.18	1.25	0.15	1.30	0.18
EF <sub>exp,cathodal</sub>	1.19	0.17	1.32	0.18	1.32	0.20
<u>EF</u> <sub>exp</sub>	1.22	0.12	1.28	0.12	1.31	0.20
Computational predictions - ele	ctric field in V/m					
EF magnitude (V/m)	Dorsal	RCE	Intermediate	RCE	Ventral	RCE
Mean	3.79	3.11	3.76	2.93	3.78	2.88
Minimum	3.04	2.50	3.07	2.39	3.01	2.29
Maximum	5.21	4.28	4.91	3.83	4.61	3.52
Percentile 95	5.02	4.12	4.81	3.75	4.47	3.42
Percentile 99	5.07	4.16	4.89	3.81	4.56	3.48
Median	3.56	2.92	3.47	2.70	3.80	2.90
StdDev	0.64	_	0.65	_	0.52	_

Table 6 Comparison between EF magnitude values determined experimentally in the spinal GM for I = 100  $\mu A$  and I = 10  $\mu A$  (number of samples for all conditions and current values is 15). Values of the ratios determined using the experimental values indicated in Table 5 for both applied current, on each experimental condition: anodal or cathodal, and dorsal, intermediate or ventral regions of the spinal GM. SE: standard error.

Experimental data - voltage gradient (Slope of linear fit)				
Experiment condition	Ratio (EF <sub>exp</sub> )	SE		
Anodal, Dorsal	6.1	1.2		
Anodal, Intermediate	7.9	2.3		
Anodal, Ventral	8.3	1.8		
Cathodal, Dorsal	8.8	2.4		
Cathodal, Intermediate	8.8	2.6		
Cathodal, Ventral	9.9	2.3		

recordings of voltage gradients during tsDCS in a living animal.

The model will allow us to design tsDCS protocols to apply in animal models so that they closely mimic the parameters of tsDCS application in humans. This is especially important in neurological diseases in which the spinal activity levels are altered such as ALS. In both symptomatic ALS patients and symptomatic SOD1 animals the spinal MNs show symptoms of intrinsic hyperexcitability [64], while in the presymptomatic stage, signs of hypoexcitability are seen [33]. Both hyper and hypoexcitability arise from a disbalance between MN intrinsic excitability and synaptic inhibition/excitation levels and tsDCS has the potential to affect both of these parameters [14,35,36]. With the newly developed DC model, we will now be able to link the geometrical parameters of the tsDCS field with the physiological effects observed at the level of spinal circuits and individual spinal motoneurons. This will further allow us to study the tsDCS-related mechanisms of neuroplasticity and design human interventions that mimic the tsDCS actions observed in mouse models.

### 4.5. Limitations and future work

Our computational model was based on a high-resolution MRI of a C57/B6 mouse, the strain available at the imaging lab, while the electrophysiological investigations were performed on SOD1 G93A mouse model of ALS. However, the background of SOD1 G93A mice is the B6SJL mice, created by crossing the C57/B6 and SJL mice. Therefore the two models are not far from each other and display no major anatomical differences. Importantly, the SOD1 G93A mice used in this study

presented no ALS motor symptoms, indicating that the motor pathways and spinal circuits were mostly intact at the time of the experiment. Therefore we do not expect that the strain of the mice significantly impacted our results, however, the differences between the segmented model and the actual experimental animals may have impacted the accuracy of the simulations. To assess the significance of anatomical variability in the computer simulations, versions of the presented 3D model with variations of animal size and tissue thickness should be designed to account for this heterogeneity factor [65].

Moreover, during the MRI segmentation and 3D modeling processes, some structures were modeled considering murine anatomy approximations (particularly subcutaneous fat, muscle, dura mater and CSF tissues). Furthermore, the ganglia roots of the SC were not included in the model, which may impact the EF distribution in the spinal canal. Future versions of the model should also include a more comprehensive range of segmented organs, such as the urinary and reproductive systems, which were omitted in the present study. This expansion would provide a more detailed anatomical representation and improve the accuracy of EF simulations for tsDCS applications targeting the lumbosacral region.

The consistent discrepancy between the experimental and computational results indicates a systematic contribution from the conductivity values used in the model. Hence, while the model's structure is likely correct, the material properties assigned to the tissues need refinement. Future studies should focus on systematically assessing tissue conductivity values, particularly for skin, fat, muscle, bone, WM, and GM, to improve simulation accuracy. For instance, a sensitivity analysis on the different tissue electric conductivity values available in the literature should be conducted to assess the influence of this factor on the EF predictions. This type of analysis has been performed on human computer models of transcranial direct current stimulation (tDCS) [66].

The systematic nature of the discrepancy between experimental and computational results also suggests that factors in the experimental setup may introduce consistent biases, considering the dispersion of the voltage deflection data (reflected by large standard deviation values in some regions). These could include slight variations in electrode positioning, tissue conductivities, or biological variability among the experimental animals. Although including the surgical opening in the model did not result in an improvement of the simulated EF magnitude along the SC, assessing the effect of other experimental set up components in the computer model will be considered.

With this work, we build a robust framework to validate an *in silico* model for tsDCS protocol optimization for experiments in the SOD1 mouse and other similar models of disease. After identifying sources of

inaccuracies, the updating of the current model to a more robust version will allow us to progress to explore the neuromodulatory potential of other electrode montages (for example, dorso-ventral montages), and input current intensity values. Furthermore, if future experimental validation confirms that the EF magnitude discrepancy is systematic, we will explore the development of a correction factor for use in computational simulations.

### CRediT authorship contribution statement

L. de Oliveira Pires: Writing – original draft, Visualization, Methodology, Investigation, Formal analysis. B. Wasicki: Visualization, Validation, Methodology, Investigation, Formal analysis. A. Abaei: Writing – original draft, Visualization, Methodology, Investigation, Formal analysis. J. Scekic-Zahirovic: Investigation. F. Roselli: Writing – original draft, Visualization, Supervision, Methodology, Investigation, Conceptualization. S. Fernandes: Writing – original draft, Supervision, Methodology, Investigation, Funding acquisition, Formal analysis, Conceptualization. M. Bączyk: Writing – original draft, Supervision, Methodology, Investigation, Funding acquisition, Formal analysis, Conceptualization.

### Support

This work was supported by JPND 2022 grant funding the DC4MND consortium. F.R. was supported by the BundesMinisterium für Forschungs und Bildgebung (BMBF) with the grant no. 01ED2301 (JPND-DC4MND) and 01ED2302 (JPND-HiCALS) and by the Deutsche ForschungsGemeinschaft (DFG) with the grants no. 443642953 and 446067541. F.R. was also supported by the German Center for Neurodegenerative Diseases (DZNE) core funding. M.B. and B.W. were supported by Polish National Science Centre grant 2022/04/Y/NZ4/00117 (JPND Call 2022), and M.B. was further supported by Polish National Science Centre grant 2019/35/B/NZ4/02058 (OPUS 35). L.d.O.P and S. R.F. are supported by FCT Fundação para a Ciência e Tecnologia under the scope of the project JPND/0003/2022 (https://doi.org/10.54499/ JPND/0003/2022) and FCT-IBEB Strategic Project UID/00645/2025. L.d.O.P was further supported by FCT Fundação para a Ciência e Tecnologia under the Bolsa de Investigação para Doutoramento 2024.00602.BD.

### Data availability statement

The data supporting the findings of this study are publicly available via Zenodo with DOI 10.5281/zenodo.15348780. The dataset is titled "Computational Modeling and Validation Data for Trans-spinal Direct Current Stimulation (tsDCS) in SOD1 Mice", and is licensed under Creative Commons Attribution 4.0 International (CC BY 4.0). All relevant files, including raw recordings from electrophysiological experiments, MRI scans, STL surface models, and FEM tetrahedral meshes, are included in the repository. Access is available upon request. Detailed metadata and usage instructions are provided in the accompanying README file.

### **Ethics statement**

The research described in this manuscript adheres to the ethical standards outlined by *Computers in Biology and Medicine* and Elsevier.

This work involves the use of animals for the experimental validation of a computational model of trans-spinal direct current stimulation (tsDCS) applied to SOD1 mice. All experimental protocols were conducted in full compliance with institutional and international ethical guidelines, including the EU Directive 2010/63/EU on the protection of animals used for scientific purposes. Ethical approval for this study was granted by the Local Ethics Committee of Poznań University of Physical Education (Poznań, Poland) under approval number 15/2024. All

procedures were designed to minimize animal discomfort and were performed by trained personnel with the necessary permits to work with laboratory animals.

This manuscript reflects original work, free from plagiarism or data manipulation. All authors have made significant contributions, reviewed, and approved the final manuscript for submission. Additionally, potential conflicts of interest and sources of funding have been transparently disclosed, in alignment with the publishing ethics policies of *Computers in Biology and Medicine* and Elsevier's standards of integrity in scientific research.

### **Declaration of competing interest**

The authors declare that they have no known competing financial interests or personal relationships that could have appeared to influence the work reported in this paper.

### Acknowledgements

We thank Msc. Piotr Zawistowski for his help in r-code for electrophysiological analysis. We thank frau dr. Diana Wiesner for the assistance with animals husbandry and frau Gizem Yartas for technical assistance.

### Glossary:

ALS Amyotrophic Lateral Sclerosis

DC direct current(s)

EF electric field(s)

I.p. Intraperitoneal injection. A way of injecting substances into a

body cavity

I.v. Intravenous injection. A way of injecting substances into a

vain

In vivo experiments performed on a living organism

Laminectomy removal of the dorsal lamina of a vertebrae

MNs motor neurons

MRI magnetic ressonance imaging

S.c. subcutaneous. A way of injecting substances under the skin Spinal nerve a bundle of nerve fibers exiting the spinal column by a single intervertebral foramen. Consists of both ventral and

dorsal root nerve fibers

SC spinal cord

SS spinal segment. Area of the spinal cord giving origin to nerve

fibers of a single spinal nerve

tsDCS trans-spinal direct current stimulation. A neuromodulation method based on applying direct current by the electrodes

placed on the skin

Voltage gradient maximum derivative of the membrane potential; vectorial quantity, with the same magnitude as the electric

field and opposite orientation

WT wild-type

### References

- G. Ardolino, T. Bocci, M. Nigro, et al., Spinal direct current stimulation (tsDCS) in hereditary spastic paraplegias (HSP): a sham-controlled crossover study, J. Spinal Cord Med. 44 (1) (2021) 46–53.
- [2] F. Cogiamanian, M. Vergari, F. Pulecchi, et al., Effect of spinal transcutaneous direct current stimulation on somatosensory evoked potentials in humans, Clin. Neurophysiol. 119 (11) (2008) 2636–2640.
- [3] F. Cogiamanian, G. Ardolino, M. Vergari, et al., Transcutaneous spinal direct current stimulation, Front. Psychiatr. 3 (2012) 63.
- [4] V. Di Lazzaro, F. Ranieri, M. Bączyk, et al., Novel approaches to motoneuron disease/ALS treatment using non-invasive brain and spinal stimulation: IFCN handbook chapter, Clin. Neurophysiol. 158 (2024) 114–136.
- [5] T. Bocci, B. Vannini, A. Torzini, et al., Cathodal transcutaneous spinal direct current stimulation (tsDCS) improves motor unit recruitment in healthy subjects, Neurosci. Lett. 578 (2014) 75–79.

- [6] L.M. Murray, B. Tahayori, M. Knikou, Transspinal direct current stimulation produces persistent plasticity in human motor pathways, Sci. Rep. 8 (1) (2018) 717
- [7] M. Guidetti, R. Ferrucci, M. Vergari, et al., Effects of transcutaneous spinal direct current stimulation (tsDCS) in patients with chronic pain: a clinical and neurophysiological study, Front Neurol. 12 (2021). (Accessed 2 August 2024).
- [8] H. Rahin, W.S. Jackson, M. Thordstein, Effect of transcutaneous spinal direct current stimulation in patients with painful polyneuropathy and influence of possible predictors of efficacy including BDNF polymorphism: a randomized, shamcontrolled crossover study, Brain Sci. 13 (2) (2023) 229.
- [9] J.-T. Lin, C.-J. Hsu, W. Dee, et al., Anodal transcutaneous DC stimulation enhances learning of dynamic balance control during walking in humans with spinal cord injury, Exp. Brain Res. 240 (7–8) (2022) 1943–1955.
- [10] A. Paget-Blanc, J.L. Chang, M. Saul, et al., Non-invasive treatment of patients with upper extremity spasticity following stroke using paired trans-spinal and peripheral direct current stimulation, Bioelectron. Med. 5 (1) (2019) 11.
- [11] M. Guidetti, S. Giannoni-Luza, T. Bocci, et al., Modeling electric fields in transcutaneous spinal direct current stimulation: a clinical perspective, Biomedicines 11 (5) (2023) 1283.
- [12] M. Hubli, V. Dietz, M. Schrafl-Altermatt, et al., Modulation of spinal neuronal excitability by spinal direct currents and locomotion after spinal cord injury, Clin. Neurophysiol. 124 (6) (2013) 1187–1195.
- [13] M. Pereira, S.R. Fernandes, P.C. Miranda, et al., Lumbar trans-spinal direct current stimulation: a modeling-experimental approach to dorsal root ganglia stimulation, Front Neurosci. 16 (2022). (Accessed 31 July 2024).
- [14] T. Jankowiak, M. Cholewiński, M. Bączyk, Differential effects of invasive anodal trans-spinal direct current stimulation on monosynaptic excitatory postsynaptic potentials, Ia afferents excitability, and motoneuron intrinsic properties between superoxide dismutase Type-1 glycine to alanine substitution at position 93 and wildtype mice, Neuroscience 498 (2022) 125–143.
- [15] E. Jankowska, Spinal control of motor outputs by intrinsic and externally induced electric field potentials, J. Neurophysiol. 118 (2) (2017) 1221–1234.
- [16] H.R. Berry, R.J. Tate, B.A. Conway, Transcutaneous spinal direct current stimulation induces lasting fatigue resistance and enhances explosive vertical jump performance, PLoS One 12 (4) (2017) e0173846.
- [17] F. Cogiamanian, M. Vergari, E. Schiaffi, et al., Transcutaneous spinal cord direct current stimulation inhibits the lower limb nociceptive flexion reflex in human beings, Pain 152 (2) (2011) 370–375.
- [18] A. Rahman, D. Reato, M. Arlotti, et al., Cellular effects of acute direct current stimulation: somatic and synaptic terminal effects, J. Physiol. 591 (10) (2013) 2563–2578.
- [19] M. Bączyk, N.O. Alami, N. Delestrée, et al., Synaptic restoration by cAMP/PKA drives activity-dependent neuroprotection to motoneurons in ALS, J. Exp. Med. 217 (8) (2020) e20191734.
- [20] S. Saxena, F. Roselli, K. Singh, et al., Neuroprotection through excitability and mTOR required in ALS motoneurons to delay disease and extend survival, Neuron 80 (1) (2013) 80–96.
- [21] M. Capogrosso, J. Gandar, N. Greiner, et al., Advantages of soft subdural implants for the delivery of electrochemical neuromodulation therapies to the spinal cord, J. Neural, Eng. 15 (2) (2018) 026024.
- [22] S. Idlett, M. Halder, T. Zhang, et al., Assessment of axonal recruitment using model-guided preclinical spinal cord stimulation in the ex vivo adult mouse spinal cord, J. Neurophysiol. 122 (4) (2019) 1406–1420.
- [23] A. Athani, N.N.N. Ghazali, I.A. Badruddin, et al., Image-based hemodynamic and rheological study of patient's diseased arterial vasculatures using computational Fluid dynamics (CFD) and fluid-structure interactions (FSI) analysis: a review, Arch. Comput. Methods Eng. 32 (3) (2025) 1427–1457.
- [24] A. Athani, N.N.N. Ghazali, I. Anjum Badruddin, et al., Visualization of multiphase pulsatile blood over single phase blood flow in a patient specific stenosed left coronary artery using image processing technique, BME 34 (1) (2023) 13–35.
- [25] P.T.J.A. Williams, D.Q. Truong, A.C. Seifert, et al., Selective augmentation of corticospinal motor drive with trans-spinal direct current stimulation in the cat, Brain Stimul. 15 (3) (2022) 624–634.
- [26] N. Zareen, M. Shinozaki, D. Ryan, et al., Motor cortex and spinal cord neuromodulation promote corticospinal tract axonal outgrowth and motor recovery after cervical contusion spinal cord injury, Exp. Neurol. 297 (2017) 179–189.
- [27] A. Wang, G. Zhang, C. Zhang, et al., Simulation of injury potential compensation by direct current stimulation in rat spinal cord, Bio Med. Mater. Eng. 24 (6) (2014) 3602–3700
- [28] S.R. Fernandes, R. Salvador, M. De Carvalho, et al., Modelling studies of non-invasive electric and magnetic stimulation of the spinal cord, in: S.N. Makarov, G. M. Noetscher, A. Nummenmaa (Eds.), Brain and Human Body Modeling 2020 [Internet], Springer International Publishing, Cham, 2021, pp. 139–165. Available from: http://link.springer.com/10.1007/978-3-030-45623-8\_8. (Accessed 18 July 2024).
- [29] S.R. Fernandes, R. Salvador, C. Wenger, et al., Transcutaneous spinal direct current stimulation of the lumbar and sacral spinal cord: a modelling study, J. Neural. Eng. 15 (3) (2018) 036008.
- [30] J. Hegedus, C.T. Putman, N. Tyreman, et al., Preferential motor unit loss in the SODI <sup>G93A</sup> transgenic mouse model of amyotrophic lateral sclerosis, J. Physiol. 586 (14) (2008) 3337–3351.
- [31] M. Bączyk, H. Drzymała-Celichowska, W. Mrówczyński, et al., Long-lasting modifications of motoneuron firing properties by trans-spinal direct current stimulation in rats, Eur. J. Neurosci. 51 (8) (2020) 1743–1755.

- [32] N. Delestrée, M. Manuel, C. Iglesias, et al., Adult spinal motoneurones are not hyperexcitable in a mouse model of inherited amyotrophic lateral sclerosis, J Physiol (Lond) 592 (7) (2014) 1687–1703.
- [33] M.D.L. Martínez-Silva, R.D. Imhoff-Manuel, A. Sharma, et al., Hypoexcitability precedes denervation in the large fast-contracting motor units in two unrelated mouse models of ALS, eLife 7 (2018) e30955.
- [34] A. Pambo-Pambo, J. Durand, J.-P. Gueritaud, Early excitability changes in lumbar motoneurons of transgenic SOD1G85R and SOD1G(93A-Low) mice, J. Neurophysiol. 102 (6) (2009) 3627–3642.
- [35] Z. Ahmed, Modulation of gamma and alpha spinal motor neurons activity by transspinal direct current stimulation: effects on reflexive actions and locomotor activity, Phys. Rep. 4 (3) (2016).
- [36] M. Bączyk, H. Drzymała-Celichowska, W. Mrówczyński, et al., Motoneuron firing properties are modified by trans-spinal direct current stimulation in rats, J. Appl. Physiol. 126 (5) (2019) 1232–1241.
- [37] P.A. Yushkevich, J. Piven, H.C. Hazlett, et al., User-guided 3D active contour segmentation of anatomical structures: significantly improved efficiency and reliability, Neuroimage 31 (3) (2006) 1116–1128.
- [38] T. Neutelings, B.V. Nusgens, Y. Liu, et al., Skin physiology in microgravity: a 3-month stay aboard ISS induces dermal atrophy and affects cutaneous muscle and hair follicles cycling in mice, npj Microgravity 1 (1) (2015) 1–9.
- [39] S. Gabriel, The dielectric properties of body tissues [internet]. http://niremf.ifac. cnr.it/docs/DIELECTRIC/Report.html#Materials, 1997. (Accessed 18 July 2024).
- [40] M.J. Peters, J.G. Stinstra, I. Leveles, The electrical conductivity of living tissue: a parameter in the bioelectrical inverse problem, in: B. He (Ed.), Modeling and Imaging of Bioelectrical Activity [Internet], Springer US, Boston, MA, 2004, pp. 281–319. Available from: http://link.springer.com/10.1007/978-0-387-49963-5 9. (Accessed 12 August 2024).
- [41] Y. Zare, K.Y. Rhee, Definition of "B" exponent and development of power-law model for electrical conductivity of polymer carbon nanotubes nanocomposites, Results Phys. 16 (2020) 102945.
- [42] L.A. Geddes, L.E. Baker, The specific resistance of biological material—A compendium of data for the biomedical engineer and physiologist, Med . biol Engng. 5 (3) (1967) 271–293.
- [43] F.L.H. Gielen, W. Wallinga-de Jonge, K.L. Boon, Electrical conductivity of skeletal muscle tissue: experimental results from different musclesin vivo, Med. Biol. Eng. Comput. 22 (6) (1984) 569–577.
- [44] J.D. Kosterich, K.R. Foster, S.R. Pollack, Dielectric permittivity and electrical conductivity of fluid saturated bone, IEEE (Inst. Electr. Electron. Eng.) Trans. Biomed. Eng. BME-30 (2) (1983) 81–86.
- [45] J. Haueisen, C. Ramon, M. Eiselt, et al., Influence of tissue resistivities on neuromagnetic fields and electric potentials studied with a finite element model of the head, IEEE (Inst. Electr. Electron. Eng.) Trans. Biomed. Eng. 44 (8) (1997) 727–735.
- [46] M. Thurai, V.D. Goodridge, R.J. Sheppard, et al., Variation with age of the dielectric properties of mouse brain cerebrum, Phys. Med. Biol. 29 (9) (1984) 1133–1136.
- [47] S.B. Baumann, D.R. Wozny, S.K. Kelly, et al., The electrical conductivity of human cerebrospinal fluid at body temperature, IEEE Trans. Biomed. Eng. 44 (3) (1997) 220–223.
- [48] M. Oozeer, C. Veraart, V. Legat, et al., Simulation of intra-orbital optic nerve electrical stimulation, Med. Biol. Eng. Comput. 43 (5) (2005) 608–617.
- [49] P. Krafft, E. Bailey, T. Lekic, et al., Etiology of stroke and choice of models, Int. J. Stroke: offic. j. Int. Stroke Soc. 7 (2012) 398–406.
- [50] A. Surowiec, S.S. Stuchly, L. Eidus, et al., In vitro dielectric properties of human tissues at radiofrequencies, Phys. Med. Biol. 32 (5) (1987) 615–621.
- [51] S. Rush, J.A. Abildskov, R. Mcfee, Resistivity of body tissues at low frequencies, Circ. Res. 12 (1) (1963) 40–50.
- [52] P.C. Miranda, A. Mekonnen, R. Salvador, et al., The electric field in the cortex during transcranial current stimulation, Neuroimage 70 (2013) 48–58.
- [53] R. Salvador, A. Mekonnen, G. Ruffini, et al., Modeling the electric field induced in a high resolution realistic head model during transcranial current stimulation, in: 2010 Annual International Conference of the IEEE Engineering in Medicine and Biology [Internet], IEEE, Buenos Aires, 2010, pp. 2073–2076. Available from: http: //ieeexplore.ieee.org/document/5626315/. (Accessed 12 August 2024).
- [54] Hadley Wickham, ggplot2: Elegant Graphics for Data Analysis [Internet], Springer-Verlag, New York, 2016. Available from: https://ggplot2.tidyverse.org.
- [55] K.W. Fishbein, K.W. Sexton, H. Celik, et al., Stabilization of T2 relaxation and magnetization transfer in cartilage explants by immersion in perfluorocarbon liquid, Magn. Reson. Med. 81 (5) (2019) 3209–3217.
- [56] P.T. Boggs, C.H. Spiegelman, J.R. Donaldson, et al., A computational examination of orthogonal distance regression, J. Econom. 38 (1) (1988) 169–201.
- [57] S. Budday, R. Nay, R. De Rooij, et al., Mechanical properties of gray and white matter brain tissue by indentation, J. Mech. Behav. Biomed. Mater. 46 (2015) 318–330.
- [58] K. Mukund, S. Subramaniam, Skeletal muscle: a review of molecular structure and function, in health and disease, WIREs Syst. Biol. Med. 12 (1) (2020) e1462.
- [59] A. Kuck, D.F. Stegeman, E.H.F. van Asseldonk, Modeling trans-spinal direct current stimulation for the modulation of the lumbar spinal motor pathways, J. Neural. Eng. 14 (5) (2017) 056014.
- [60] M. Parazzini, S. Fiocchi, I. Liorni, et al., Modeling the current density generated by transcutaneous spinal direct current stimulation (tsDCS), Clin. Neurophysiol. 125 (11) (2014) 2260–2270.
- [61] M.A. Nitsche, W. Paulus, Excitability changes induced in the human motor cortex by weak transcranial direct current stimulation, J. Physiol. 527 (3) (2000) 633–639.

- [62] P. Marangolo, V. Fiori, C. Caltagirone, et al., Stairways to the brain: transcutaneous spinal direct current stimulation (tsDCS) modulates a cerebellar-cortical network enhancing verb recovery, Brain Res. 1727 (2020) 146564.
- [63] S.R. Fernandes, Transcutaneous spinal direct current stimulation: modelling the spinal electric field distribution and clinical relevance [Internet] [doctoralThesis]. Available from: https://repositorio.ul.pt/handle/10451/55166, 2019. (Accessed 9 August 2024).
- [64] D.B. Jensen, M. Kadlecova, I. Allodi, et al., Spinal motoneurones are intrinsically more responsive in the adult G93A SOD1 mouse model of amyotrophic lateral sclerosis, J. Physiol. 598 (19) (2020) 4385–4403.
- [65] Y. Huang, A.A. Liu, B. Lafon, et al., Measurements and models of electric fields in the in vivo human brain during transcranial electric stimulation, eLife 6 (2017) e18834.
- [66] L. Santos, M. Martinho, R. Salvador, et al., Evaluation of the electric field in the brain during transcranial direct current stimulation: a sensitivity analysis, Annu. Int. Conf.IEEE Eng. Med. Biol. Soc. 2016 (2016) 1778–1781.